Mathematics, Computation and Geometry of Data
Volume 2, Number 2, 117–149, 2022

A geometric variational framework for computing spherical optimal transportation maps II

Zhou Zhao, Na Lei, Li Cui, Kehua Su, Xiaoyin Xu, Feng Luo, Xianfeng Gu*, and Shing-Tung Yau

Optimal transportation maps play fundamental roles in many engineering and medical fields. The computation of optimal transportation maps can be reduced to solve highly non-linear Monge-Ampère equations.

This work summarizes the geometric variational frameworks for spherical optimal transportation maps, which offers solutions to the Minkowski problem in convex differential geometry, reflector design and refractor design problems in optics. The method is rigorous, robust and efficient. The algorithm can directly generalized to higher dimensions.

1. Introduction

Optimal transportation (OT) map finds the most economical way to transfer one probability measure to another. The transportation cost gives a metric among measures – the so-called Wasserstein metric. Optimal transportation method has become an important tool in optics [11], economy [10] and life science [24]. Recently, OT has been successfully applied in different areas of computer science, such as parameter estimation in Bayesian nonparametric models [21], computer vision [4, 8, 27], natural language processing [16, 30], medical image registration [15], 3D surface registration [25, 17, 32, 14], color transfer [9, 22, 23] and so on. The Wasserstein metric has also been broadly applied in generative models in deep learning, such as the WGAN model [4, 20], WAE [27], AE-OT [2, 3], and energy-based models [1].

The origin of the optimal transport problem can be traced back to 1781, when Monge asked if there existed an OT map between two measures for a given cost function. Depending on the cost function and the measures, the OT map may not exist. In the 1950s, Kantorovich relaxed the OT map to OT plan, and showed the existence and the uniqueness of the plan under mild conditions [29]. In the 1980s, Brenier [7] discovered that, when the

*Corresponding author.

density of the source measure is absolutely continuous and the cost function is the squared Euclidean distance, the OT map is given by the gradient of a convex function, the so-called Brenier potential.

Recently, the equivalence between the Brenier potential and Alexandrov's convex polytope has been proved in [13], as both of them can be obtained by solving the non-linear Monge-Ampère equation. This connection leads to a practical algorithm to solve the semi-discrete OT problem using convex geometry. According to the Brenier theorem, the Brenier potential can be represented as the upper envelope of a set of hyperplanes, and its projection induces a power diagram of the source domain, which gives the semi-discrete OT map. The geometric variational method proposed by Su et al. [25] is based on classical computational geometry [6] and solves the semi-discrete OT problem by minimizing a convex energy. Though with high accuracy, the method is very slow and inefficient. At each step, it constructs a new power diagram, or a weighted Delaunay triangulation of the samples. During the optimization, the combinatorial structures of the triangulation are changed dynamically, which makes the algorithm complicate. Moreover, as the method assumes that the source distribution is uniform, it cannot handle complex source measures. To circumvent this limitation, we can generalize the Lawson's edge flip algorithm [18] to update the power diagram during the optimization, instead of constructing a new convex hull at each iteration like Su et al. did in [25]. This improves the computational efficiency by a factor of more than 5. To handle the piecewise linearly defined source measures, we can use the sweep convex polygon algorithm, which is a generalization of the classical Bentley-Ottman's sweep line algorithm [5], to compute the subdivision of two cell decompositions. Thus we can compute the semi-discrete OT map from a piecewise linear source measure to the target measure. This improves the efficiency and the robustness of the algorithm.

Within the same framework of the OT solution, we can extend the OT problem to solve the worst transportation (WT) problem [31], which tries to maximize the cost between two distributions, given a cost function between them. Different from finding the convex Brenier potential for the OT problem, the WT problem finds the concave Brenier potential whose gradient gives the WT map. Moreover, we can unify the OT solution and WT solution into a single framework and solve them by Newton's method. We also discover the intrinsic symmetry between the OT map and the WT map.

The geometric variational framework is generalizable for any dimensions. For example, volumetric optimal transportation maps can also be directly computed based on the same principle. However, the volumetric computational algorithms are more complicated than planar ones.

2. Theoretic foundation

This section introduces the theoretic foundation of our geometric variational framework for spherical optimal transportation maps. For more details for general optimal transportation theory, we refer readers to [28, 29, 19].

2.1. Continuous Minkowski problem of type I

We introduce the classical Minkowski problem of type I, which is closely related to the spherical optimal transportation.

As shown in Fig. 1, suppose $K \subset \mathbb{R}^d$ is a bounded open convex domain, containing the origin, the boundary ∂K is parameterized by polar coordinates:

$$\partial K = \{\rho(x)x : x \in \mathbb{S}^{d-1}, \rho : \mathbb{S}^{d-1} \to \mathbb{R}^+\}.$$

Definition 2.1 (sub-normal map)**.** For any point $z \in \partial K$, the *sub-normal map* maps a point z to a closed set on the unit sphere, $z \mapsto N_K(z)$,

$$N_K(z) := \left\{ y \in \mathbb{S}^{d-1} : K \subset \{w : \langle y, w - z\rangle \leq 0\} \right\}. \tag{2.1}$$

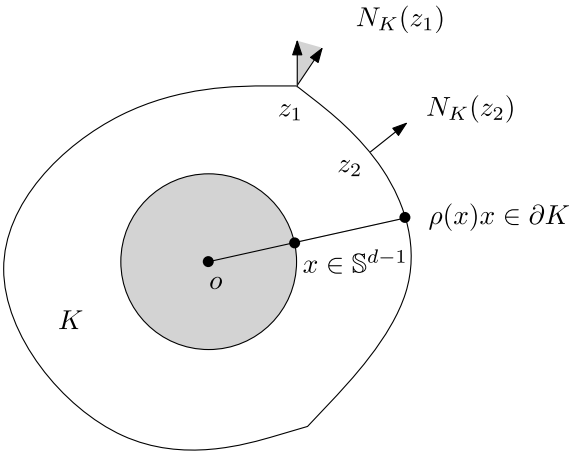

Figure 1: Given a convex $K \ni 0$, the boundary ∂K is parameterized by polar coordinates, represented as $\rho : \mathbb{S}^{d-1} \to \mathbb{R}^+$. Given a point $z \in \partial K$, the set $N_K(z)$ consists of all the exterior normals at z. When K has a unique tangent plane at z (such as z_2), $N_k(z)$ is a singleton. If z is a corner point, then $N_K(z)$ consists of multiple elements (such as z_1).

Definition 2.2 (Gauss Map)**.** The multi-valued Gauss map $G_K : \mathbb{S}^{d-1} \to \mathbb{S}^{d-1}$ is defined by:

$$G_K(x) := N_K(\rho(x)x).$$

The Gauss curvature measure is defined as:

$$\mu_K(E) := \mathcal{H}^{d-1}(G_K(E)), \quad \forall \text{ Borel set } E \subset \mathbb{S}^{d-1}.$$

where $\mathcal{H}^{d-1}$ represents the $d-1$ dimensional Hausdorff measure on $\mathbb{S}^{d-1}$. □

It can be shown that μ_K is a Borel measure. As shown in Fig. 2, the Minkowski problem is formulated as follows:

Problem 2.3 (Minkowski I)**.** Given a Borel measure ν defined on the sphere $\mathbb{S}^{d-1}$, can we find a bounded convex open set $K \ni 0$, such that $\nu = \mu_K$? □

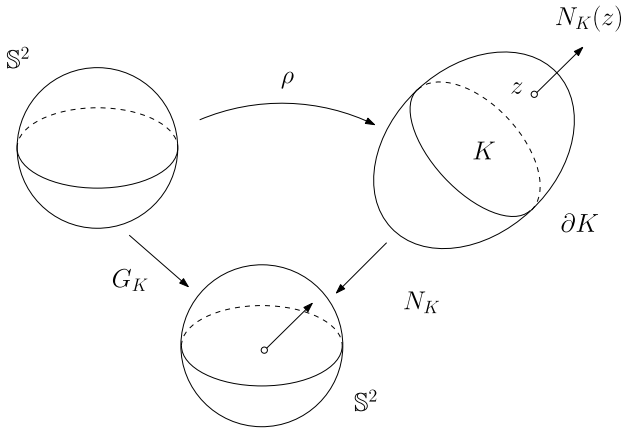

Figure 2: Minkowski Problem I.

The answer to the Minkowski problem is positive.

2.1.1. Minkowski theorem

Definition 2.4 (Spherical Convex Set and Polar Set)**.** Given a spherical set $\omega \subset \mathbb{S}^{d-1}$, we say ω is convex, if the cone

$$\mathbb{R}^+\omega := \{tx : t > 0, x \in \omega\}$$

is convex. The polar set of ω is defined as

$$\omega^* := \{y \in \mathbb{S}^{d-1} : \langle x, y\rangle \leq 0, \forall x \in \omega\}.$$ □

Theorem 2.5 (Minkowski I)**.** *Let ν be a Borel measure on $\mathbb{S}^{d-1}$, then there exists a bounded convex open set K, such that*

$$\nu = \mu_K \iff \begin{cases} (a)\ \nu(\mathbb{S}^{d-1}) = \mathcal{H}^{d-1}(\mathbb{S}^{d-1}); \\ (b)\ \nu(\mathbb{S}^{d-1} \setminus \omega) > \mathcal{H}^{d-1}(\omega^*), \forall \omega \subsetneq \mathbb{S}^{d-1} \text{ compact convex.} \end{cases}$$

If K exists, then different solutions differ by a dilation. □

The regularity of the solution to the Minkowski problem is summarzied as follows:

Theorem 2.6 (Regularity of the Solution to Minkowski Problem)**.** *Suppose $K \subset \mathbb{R}^3$ is a convex open set containing the origin, if $\mu_K = f d\mathcal{H}^2$, the density function $f : \mathbb{S}^2 \to \mathbb{R}^+$ is bounded, then ∂K is C^1.* □

2.1.2. Proof of Minkowski theorem Fig. 3 shows the concept of the generalized Legendre dual:

Definition 2.7 (Spherical Legendre Dual)**.** Given a hyper-surface in $\mathbb{R}^d$, with polar representation $S := \{\rho(x)x : x \in \mathbb{S}^{d-1}, \rho : \mathbb{S}^{d-1} \to \mathbb{R}^+\}$, its spherical Legendre dual is $S^* := \{h(y)y : y \in \mathbb{S}^{d-1}, h : \mathbb{S}^{d-1} \to \mathbb{R}^+\}$, where

$$h(y) := \sup_{x \in \mathbb{S}^{d-1}} \rho(x)\langle x, y\rangle. \tag{2.2}$$

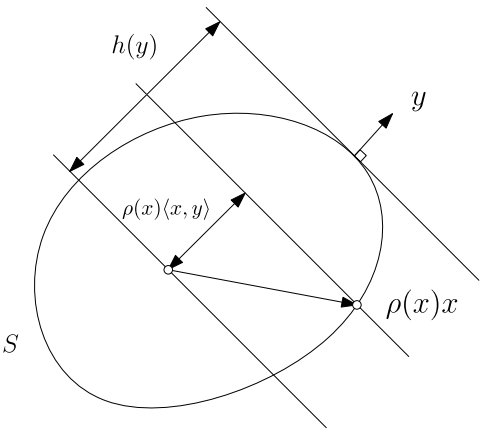

Figure 3: Generalized Legendre Transform, $h(y) = \max\{\rho(x)\langle x, y\rangle, x \in \mathbb{S}^{d-1}\}$.

symmetrically, $S = (S^*)^*$, furthermore

$$\rho(x) = \inf_{y\in\mathbb{S}^{d-1}} \frac{h(y)}{\langle x, y\rangle}, \tag{2.3}$$

or equivalently

$$\rho^{-1}(x) = \sup_{y\in\mathbb{S}^{d-1}} h^{-1}(y)\langle x, y\rangle. \qquad \square$$

Take logarithm of spherical Legendre duality formula,

$$\log\rho(x) = \inf_y \left\{ -\log\langle x, y\rangle - \log\frac{1}{h(y)} \right\}, \tag{2.4}$$

and

$$\log\frac{1}{h(y)} = \inf_x \left\{ -\log\langle x, y\rangle - \log\rho(x) \right\}. \tag{2.5}$$

Define cost function $c : \mathbb{S}^{d-1} \times \mathbb{S}^{d-1} \to \mathbb{R}^+ \cup \{0\}$,

$$c(x, y) := -\log\langle x, y\rangle, \tag{2.6}$$

then $\log\rho(x)$ and $-\log h(y)$ are c-transform of each other:

$$(\log\rho(x))^c = \log\frac{1}{h(y)} \quad \text{and} \quad \left(\log\frac{1}{h(y)}\right)^{\bar{c}} = \log\rho(x).$$

We can use spherical optimal transportation theory to prove Minkowski's theorem:

Proof. Minkowski problem I can be rephrased as an optimal transportation problem: given a Borel measure ν on $\mathbb{S}^{d-1}$, find an optimal transportation map $T : (\mathbb{S}^{d-1}, \mathcal{H}^{d-1}) \to (\mathbb{S}^{d-1}, \nu)$,

$$\min_{T_\#\mathcal{H}^{d-1}=\nu} \int_{\mathbb{S}^{d-1}} -\log\langle x, T(x)\rangle d\mathcal{H}^{d-1}.$$

this is equivalent to the dual problem:

$$\max\left\{ \int_{\mathbb{S}^{d-1}} \varphi(x)d\mathcal{H}^{d-1}(x) + \int_{\mathbb{S}^{d-1}} \varphi^c(y)d\nu(y), \quad \varphi \in c\text{-conv}\left(\mathbb{S}^{d-1}\right) \right\}.$$

the cost function $-\log\langle x, y\rangle$ is continuous, $\mathbb{S}^{d-1}$ is a compact metric space, by (DP) theory, there exists a solution $(\varphi, \varphi^c) = (\rho(x), 1/h(y))$. $\square$

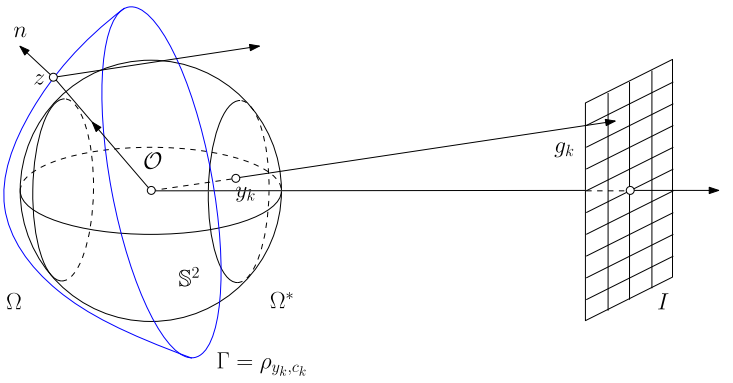

Figure 4: Reflector system set up.

2.2. Reflector design

As shown in Fig. 4, a illumination system consists of a point light source at $\mathcal{O}$ and a reflector surface Γ with polar representation,

$$\Gamma_\rho = \{x\rho(x); x \in \Omega\}, \quad \rho > 0, \tag{2.7}$$

all the incidence light rays fall inside the input domain Ω. If we only consider the far field problem, then we can only care about the directions of the reflected rays. All the reflected rays fall in the output domain Ω^*.

Figure 5: Left: the desired far field image, Lena; Right: the simulated reflected image.

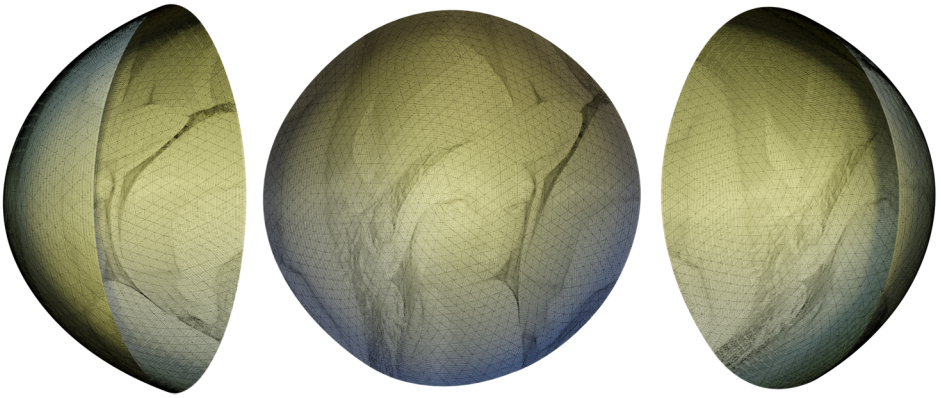

Figure 6: The reflector surface for the Lena image.

Figure 7: Left: the desired far field image, Monge; Right: the simulated reflected image.

Suppose f is the illumination intensity defined on the input domain Ω, namely the distribution of the incidence rays emanating from $\mathcal{O}$, g is the illumination intensity in the output domain Ω^*. Assume there is no energy loss, then according energy conservation law, we have

$$\int_{\Omega} f = \int_{\Omega^*} g. \tag{2.8}$$

A ray emanates from $\mathcal{O}$, propagates along a direction $x \in \Omega$, intersects the mirror at $z = x\rho(x) \in \Gamma_\rho$, the reflection direction is determined by the reflection law,

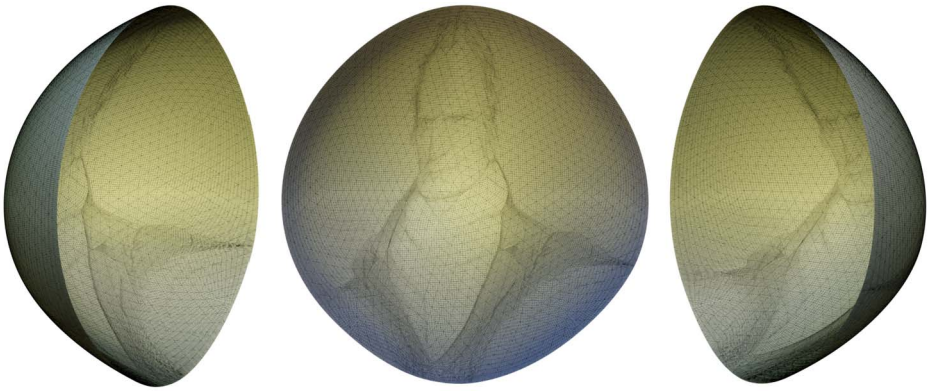

Figure 8: The reflector surface for the Monge image.

$$T(x) = T_\rho(x) = \partial\rho(x) = x - 2\langle x, n\rangle n, \tag{2.9}$$

where n is the exterior normal to the reflector surface Γ_ρ at point z, $\langle x, n\rangle$ represents the inner product. By energy conservation, T is measure preserving,

$$\int_{T^{-1}(E)} f = \int_E g, \quad \forall \text{ Borel set } E \subset \Omega^*. \tag{2.10}$$

satisfying the natural boundary condition

$$T_\rho(\Omega) = \partial\rho(\Omega) = \Omega^*. \tag{2.11}$$

By measure preserving condition, we can obtain the PDE for the reflector. In fact, at $x \in \Omega$, the Jacobi of T equals to $f(x)/g(T(x))$, in a local ortha-normal coordinates of $\mathbb{S}^2$, the local representation of the PDE is

$$\mathcal{L}\rho = \eta^{-2}\det(-\nabla_i\nabla_j\rho + 2\rho^{-1}\nabla_i\rho\nabla_j\rho + (\rho - \eta)\delta_{ij}) = f(x)/g(T(x)), \tag{2.12}$$

where ∇ is the covariant differential operator, $\eta = (|\nabla\rho|^2 + \rho^2)/2\rho$, and δ_{ij} is the Kronecker function. This is a non-linear Monge-Ampère PDE, a natural boundary condition is

$$T_\rho(\Omega) = \partial\rho(\Omega) = \Omega^*. \tag{2.13}$$

Problem 2.8 (Reflector Design)**.** Given spherical domains Ω, $\Omega^* \subset \mathbb{S}^2$, and density functions $f : \Omega \to \mathbb{R}_+$ and $g : \Omega^* \to \mathbb{R}_+$, find a reflector surface Γ_ρ,

such that the reflection map T_ρ satisfies the measure-preserving condition and the natural boundary condition.

2.2.1. Surface with uniform reflection property The uniform reflection property of a paraboloid of revolution: all the reflected rays of the incidence rays parallel to the rotation axis intersect at the focal point, vice versa, as shown in Fig. 9.

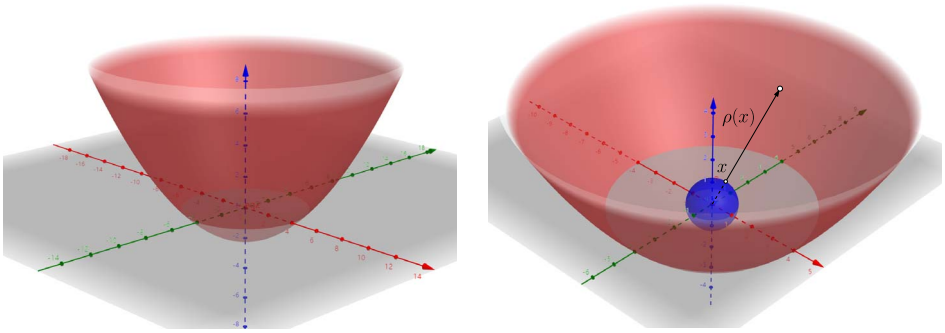

Figure 9: A paraboloid of revolution about the axis of direction y, with radial representation $\rho(x) = C/(1 - \langle x, y\rangle)$.

Definition 2.9 (Supporting Paraboloid)**.** Let $\rho \in C(\Omega)$ be a positive function, $\Gamma_\rho = \{x\rho(x) : x \in \Omega\}$ represents the radial graph of ρ. We say Γ_p is a supporting paraboloid of ρ at $x_0\rho(x_0) \in \Gamma_\rho$, where $p = p_{y,C}$, if

$$\begin{cases} \rho(x_0) = p_{y,C}(x_0), \\ \rho(x) \le p_{y,C}(x), \quad \forall x \in \Omega. \end{cases} \tag{2.14}$$

Definition 2.10 (Admissible Function)**.** We say ρ is an *admissible function*, if its radial graph Γ_ρ has a supporting paraboloid at every point.

2.3. Generalized solution

Definition 2.11 (Subdifferential)**.** Let ρ be an admissible function; the subdifferential is a set-valued map $\partial\rho : \Omega \to \mathbb{S}^2$: for any $x_0 \in \Omega$, $\partial\rho(x_0)$ is set of y_0, such that there exists a $C > 0$, $p_{y_0,C}$ is the supporting paraboloid of ρ at x_0,

$$\partial\rho(x) = \{y \in \Omega^* : \exists\ C > 0 \text{ s.t. paraboloid } p_{y,C} \text{ supports } \rho \text{ at } x\}\,. \qquad \square$$

Definition 2.12 (Generalized Alexandrov Measure)**.** The subdifferential $\partial\rho$ induces a measure $\mu = \mu_{\rho,g}$ on Ω, where $g \in L^1(\Omega^*)$ is a non-negative measurable function on $\mathbb{S}^2$, such that for any Borel set $E \subset \Omega$,

$$\mu_{\rho,g}(E) = \int_{\partial\rho(E)} g(x)dx. \tag{2.15}$$

$\mu_{\rho,g}$ is called a generalized Alexandrov measure. □

Definition 2.13 (Generalized Solution)**.** Admissible function ρ is called the generalized solution to the spherical Monge-Ampère equation for reflection system, if as measures $\mu_{\rho,g} = f dx$. Equivalently, for any Borel set $E \subset \Omega$, we have

$$\int_E f = \int_{\partial\rho(E)} g. \tag{2.16}$$

Furthermore, if ρ satisfies

$$\Omega^* \subset \partial\rho(\Omega), \quad |\{x \in \Omega : f(x) > 0 \text{ and } \partial\rho(x) - \overline{\Omega^*} \neq \emptyset\}| = 0, \tag{2.17}$$

then ρ is the generalized solution to the spherical Monge-Ampère equation for the OT map $\mathcal{L}\rho = f/g \circ T$ with natural boundary condition $T_\rho(\Omega) = \Omega^*$.

2.4. Solution to the reflector design problem

Suppose ρ is admissible, fix a direction $y \in \mathbb{S}^2$, there exists a paraboloid of revolution about the axis of direction y, represented as $p_{y,c}$ with radial representation $\frac{c}{1-\langle x,y\rangle}$, which supports Γ_ρ at point $\rho(x)x$. As shown in the Fig. 10, for any paraboloid of revolution about the axis of direction y $p_{y,\tilde{c}}$, which intersects Γ_ρ, we have $\tilde{c} \leq c$. Assume Γ_ρ intersects $p_{y,\tilde{c}}$ at $\rho(x)x$, then $\rho(x) = \frac{\tilde{c}}{1-\langle x,y\rangle}$, $\tilde{c} = \rho(x)(1 - \langle x, y\rangle)$. Hence we have

$$c(y) = \sup_{x\in\Omega} \rho(x)(1 - \langle x, y\rangle) \iff \frac{1}{c(y)} = \inf_{x\in\Omega} \frac{1}{\rho(x)(1 - \langle x, y\rangle)},$$

We represent it as $\eta : \Omega^* \to \mathbb{R}_+$, $\eta(y) = 1/c(y)$.

Definition 2.14 (Generalized Legendre Transform)**.** Suppose ρ is an admissible function defined on $\Omega \subset \mathbb{S}^2$, the generalized Legendre transform of ρ with respect to the function $\frac{1}{1-\langle x,y\rangle}$ is a function η defined on $\mathbb{S}^2$,

$$\eta(y) = \inf_{x\in\Omega} \frac{1}{\rho(x)(1 - \langle x, y\rangle)}. \tag{2.18}$$

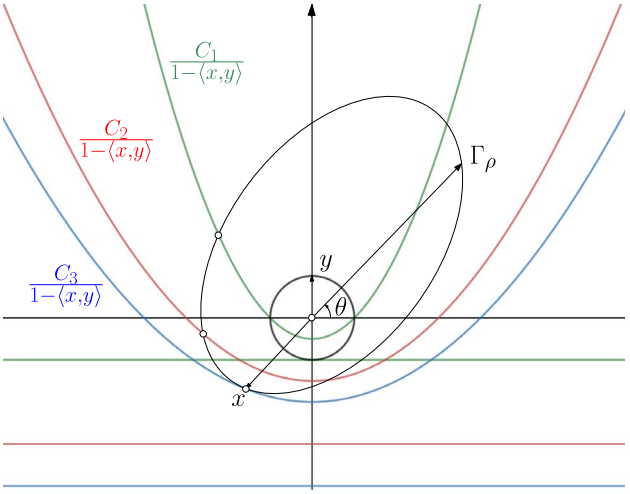

Figure 10: Generalized Legendre transformation.

For any fixed $y_0 \in \Omega^*$, suppose the infimum is reached at $x_0 \in \Omega$, hence we have

$$\eta(y_0)\rho(x_0) = \frac{1}{1-\langle x_0, y_0\rangle}, \tag{2.19}$$

for arbitrary $x \in \Omega$ and $y \in \Omega^*$,

$$\rho(x)\eta(y) \le \frac{1}{1-\langle x, y\rangle}, \tag{2.20}$$

and the paraboloid $p_{y_0,C}(x) = \frac{C}{1-\langle x,y_0\rangle}$ supports ρ at x_0, and $p_{x_0,C}(y) = \frac{C}{1-\langle x_0,y\rangle}$ supports η at y_0.

Furthermore:

$$y_0 \in \partial\rho(x_0) \iff x_0 \in \partial\eta(y_0).$$

especially, when the generalized Legendre transform of η is restricted on Ω, it is exactly ρ,

$$\rho^{**} = \rho.$$

If ρ is smooth and satisfies the Monge-Ampère equation (2.12), then the subdifferential $\partial\eta$ is the inverse map of $\partial\rho$. Hence, η satisfies the equation

$$\mathcal{L}\rho = \frac{f(x)}{g(\partial\rho(x))}, \quad \mathcal{L}\eta = \frac{g(y)}{f(\partial\eta(x))}, \tag{2.21}$$

Theorem 2.15 (Reflector Design)**.** *Suppose Ω and Ω^* are domains contained in the north and the south hemi-sphere respectively, f and g are bounded positive functions, $\int_\Omega f(x) = \int_{\Omega^*}$, then there exist a pair of functions (φ_1, ψ_1) maximizing the following energy,*

$$\sup\left\{\int_\Omega \varphi(x)f(x)dx + \int_{\Omega^*} \psi(y)g(y)dy, \varphi(x) + \psi(y) \le c(x,y)\right\}, \tag{2.22}$$

where

$$c(x,y) = -\log(1 - \langle x, y\rangle), \tag{2.23}$$

$\langle x, y\rangle$ is the inner product in $\mathbb{R}^3$, such that $\rho = e^\varphi$ is the solution to the spherical Monge-Ampère equation $\mathcal{L}\rho = f/g \circ \partial\rho$ satisfying the natural boundary condition $\partial\rho(\Omega) = \Omega^*$, and all such solutions ϕ differ by a constant. □

Proof. Reflector design is an optimal transport problem. By the existence and the uniqueness of the solution to the dual problem (DP), we get that there exist a pair of Kantorovich potentials (φ, ψ), $\psi = \varphi^c$, $\varphi = \psi^{\bar{c}}$,and φ is unique up to a constant. Let $x_0 \in \Omega$ be a differentiable point of φ,let $y_0 \in \overline{\Omega^*}$, such that

$$\begin{cases} \varphi(x_0) &= c(x_0, y_0) - \psi(y_0) \\ \varphi(x) &\le c(x, y_0) - \psi(y_0), \quad \forall x \in \Omega. \end{cases}$$

now let $\rho = e^\varphi$, the paraboloid is given by

$$p(x) = \exp(c(x, y_0) - \psi(y_0)) = \frac{C}{1 - \langle x, y_0\rangle}, C = \exp(-\psi(y_0)).$$

then $p(x)$ supports Γ_ρ at x_0.

Γ_ρ is the inner envelope of the supporting paraboloids, ρ is almost everywhere differentiable. At the differentiable points of ρ,the supporting paraboloid is unique, hence y_0 is unique. Hence, the optimal transport plan becomes an optimal transport map $T_\rho : \Omega \to \Omega^*$.

The paraboloid $p(x)$ and Γ_ρ share the same normal vector at the tangential point, by the uniform reflection property of the paraboloid, we have

$$y_0 = T_\rho(x_0) = T_p(x_0) = x_0 - 2\langle x_0, n\rangle n.$$

T_ρ is measure preserving, satisfies the spherical Monge-Ampère equation, $\mathcal{L}\rho = f/g \circ \partial\rho$, with the natural boundary condition $T_\rho(\Omega) = \Omega^*$. □

Fig. 5 and Fig. 6 show the solution to the reflector design problem, where the target image is the Lena image. Fig. 7 and Fig. 8 show the solution to the reflector design problem, where the target image is the Monge image.

2.5. Refractor design

As shown in Fig. 11, suppose n_1 and n_2 are refractive indices of two homogeneous, isotropic media I and II. Suppose the light source is at a point $\mathcal{O}$ in the medium I, along a direction $x \in \Omega \subset \mathbb{S}^2$, the light intensity is $f(x)$.

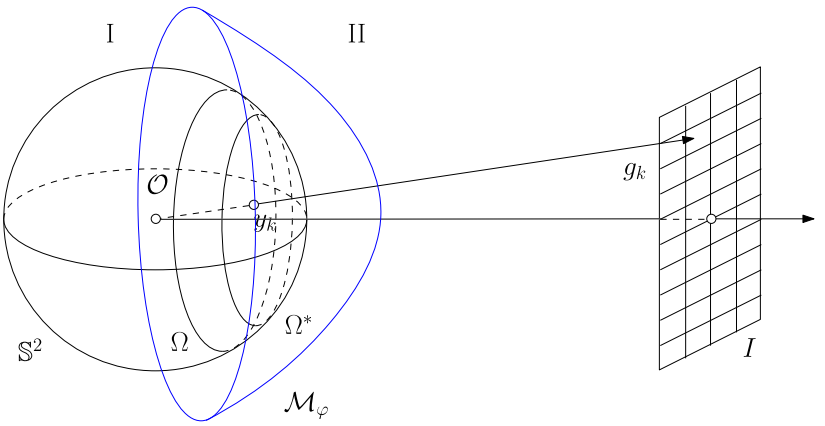

Figure 11: Refractive lens system.

We want to construct a refractive surface with radial representation Γ_ρ,

$$\Gamma_\rho = \{x\rho(x); x \in \Omega\}, \quad \rho > 0, \tag{2.24}$$

Γ_ρ separates the media I and II, such that all the directions of the refracted rays in the medium II are inside $\Omega^* \subset \mathbb{S}^2$, and the intensity of the ray along $y \in \Omega^*$ equals to $g(y)$, where the spherical function $g : \Omega^* \to \mathbb{R}$ is prescribed.

Suppose the refraction has no energy loss, by energy conservation law,

$$\int_\Omega f(x)dx = \int_{\Omega^*} g(y)dy. \tag{2.25}$$

A ray starts from $\mathcal{O}$ and arrives at $x\rho(x) \in \Gamma_\rho$, where $x \in \Omega$. It is refracted, the direction of the refracted ray is

$$T(x) = T_\rho(x) = \partial\rho(x). \tag{2.26}$$

By energy conservation, T is measure preserving, namely

$$\int_{T^{-1}(E)} f(x)dx = \int_E g(y)dy, \quad \forall \text{ Borel set } E \subset \Omega^*, \tag{2.27}$$

with natural boundary condition

$$T_\rho(\Omega) = \partial\rho(\Omega) = \Omega^*. \tag{2.28}$$

Problem 2.16 (Refractor Design)**.** Suppose n_1 and n_2 are refractive indices of two homogeneous, isotropic media. Given spherical domains $\Omega, \Omega^* \subset \mathbb{S}^2$, density functions $f : \Omega \to \mathbb{R}_+$ and $g : \Omega^* \to \mathbb{R}_+$, find refractive surface Γ_ρ separates the two media, the refraction map T_ρ (2.26) satisfies the measure preserving condition (2.27) and the natural boundary condition (2.28). □

2.5.1. Surface with uniform refraction property As shown in Fig. 12, v_1 and v_2 are the light speeds in the media I and II, $n_1 = c/v_1$, $n_2 = c/v_2$ are the *refractive indices*. Suppose a ray along the direction $x \in \mathbb{S}^{n-1}$ travels in medium I, and hits a boundary point $p \in \Gamma$ and enters the medium II, the refracted ray is along the direction $y \in \mathbb{S}^{n-1}$.

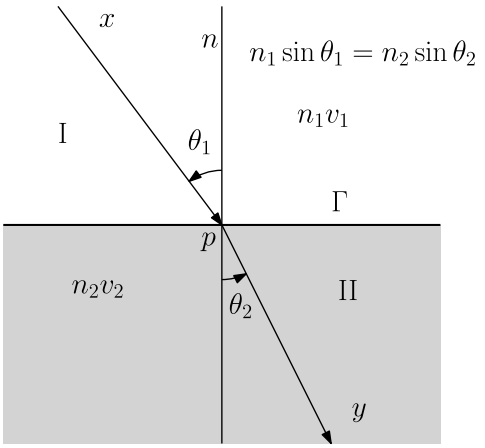

Figure 12: Snell refraction law.

Snell law claims

$$n_1 \sin\theta_1 = n_2 \sin\theta_2,$$

where θ_1 is the *angle of incidence*, θ_2 is the *angle of refraction*, n is normal to the interface surface Γ, pointing to the medium II. The vectors x, n and y are co-planar.

Definition 2.17 (Surface with uniform refraction property)**.** If the interface surface Γ of the media I and II refracts all the rays of light emanating from the origin $\mathcal{O}$ inside medium I into rays parallel to a fixed $y \in \mathbb{S}^2$, then Γ is called a surface with uniform refraction property.

$\kappa = n_2/n_1$, when $\kappa < 1$, Γ is an ellipsoid of revolution about the axis of direction y, denoted as $e_{y,b}$

$$e_{y,b} = \left\{ \rho(x)x : \rho(x) = \frac{b}{1 - \kappa\langle y, x\rangle}, x \in \mathbb{S}^{n-1}, \langle x, y\rangle \geq \kappa \right\}. \tag{2.29}$$

when $\kappa > 1$, by physics constraint $\langle x, y\rangle > 1/k$, Γ is a the sheet with opening in direction y of a hyperboloid of revolution of two sheets about the axis of direction y, as shown in Fig. 13,

$$h_{y,b} = \left\{ \rho(x)x : \rho(x) = \frac{b}{\kappa\langle y, x\rangle - 1}, x \in \mathbb{S}^{n-1}, \langle x, y\rangle \geq 1/\kappa \right\}. \tag{2.30}$$

Lemma 2.18 (Lemma)**.** *Suppose n_1 and n_2 are the refractive indices of two media I and II respectively, and $\kappa = n_2/n_1$. The origin $\mathcal{O}$ is in medium I, $e_{y,b}$ and $h_{y,b}$ are interface surface between media I and II, defined by (2.29) and (2.30) respectively, we have*
if $\kappa < 1$, then $e_{y,b}$ refracts all the rays emanating from the origin $\mathcal{O}$ in medium I into rays in medium II with refraction direction y;
if $\kappa > 1$, then $h_{y,b}$ refracts all the rays emanating from the origin $\mathcal{O}$ in medium I into rays in medium II with refraction direction y. □

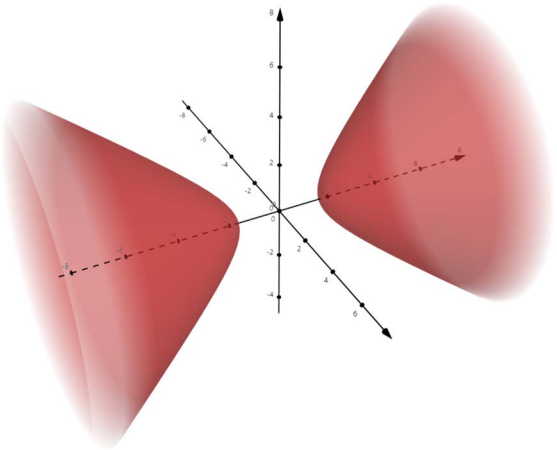

Figure 13: A hyperboloid of revolution of two sheets.

2.5.2. Generalized solution

Definition 2.19 (Supporting Ellipsoid)**.** Suppose $\rho \in C(\Omega)$ is a positive function, and $\Gamma_\rho = \{x\rho(x) : x \in \Omega\}$ is the radial graph of ρ. Let $e = e_{y,c}$ be an ellipsoid of revolution, its radial graph be Γ_e. If

$$\begin{cases} \rho(x_0) = e_{y,c}(x_0), \\ \rho(x) \le e_{y,c}(x), \quad \forall x \in \Omega, \end{cases} \tag{2.31}$$

then we say Γ_e is a *supporting ellipsoid* of ρ at the point $x_0\rho(x_0) \in \Gamma_\rho$.

If the radial graph Γ_ρ has a supporting ellipsoid at every point, then we say ρ is *admissible*.

Definition 2.20 (sub-differential)**.** Let ρ be an admissible function. We define a set-valued map $\partial\rho : \Omega \to \mathbb{S}^2$, the so-called *sub-differential*. For any $x_0 \in \Omega$, $\partial\rho(x_0)$ is the set of y_0's, such that $\exists c > 0$, $e_{y_0,c}$ is the supporting ellipsoid of ρ at x_0,

$$\partial\rho(x_0) := \{y_0 \in \mathbb{S}^2 : \exists c > 0, e_{y_0,c} \text{ supports } \rho \text{ at } x_0\}.$$

For any subset $E \subset \Omega$, we define

$$\partial\rho(E) = \bigcup_{x \in E} \partial\rho(x).$$

Definition 2.21 (Generalized Alexandrov Measure)**.** Suppose ρ is an admissible function defined on $\Omega \subset \mathbb{S}^2$, $g \in L^1(\Omega^*)$ is a non-negative measurable function defined on $\Omega^* \subset \mathbb{S}^2$, the generalized Alexandrov measure induced by ρ and g, denoted as $\mu_{\rho,g}$, is defined as

$$\mu_{\rho,g}(E) = \int_{\partial\rho(E)} g(x)dx, \quad \forall \text{ Borel } E \subset \Omega. \tag{2.32}$$

Definition 2.22 (Generalized Solution)**.** Given spherical measures $f \in L^1(\Omega)$ and $g \in L^1(\Omega^*)$, such that $\int_\Omega f dx = \int_{\Omega^*} g dy$. Suppose ρ is a spherical admissible function. If the generalized Alexandrov measure induced by ρ satisfies $\mu_{\rho,g} = f dx$, namely

$$\int_E f = \int_{\partial\rho(E)} g, \quad \forall \text{ Borel } E \subset \Omega \tag{2.33}$$

furthermore, if ρ satisfies

$$\Omega^* \subset \partial\rho(\Omega), \quad |\{x \in \Omega : f(x) > 0 \text{ and } \partial\rho(x) - \overline{\Omega^*} \neq \emptyset\}| = 0, \tag{2.34}$$

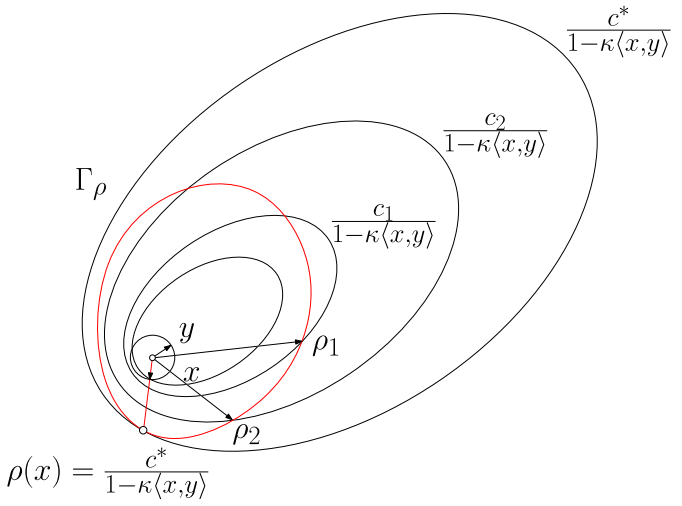

Figure 14: Generalized Legendre transform.

then we say ρ is a generalized solution to the spherical Monge-Ampère equation with natural boundary condition. □

2.5.2.1. Generalized Legendre transform As shown in Fig. 14, among all ellipsoids $e_{y,c}$'s of revolution about the axis of direction y intersecting with Γ_ρ, $c \leq c^*$. If Γ_ρ intersects $e_{y,c}$ at $\rho(x) = \frac{c}{1-\kappa\langle x,y\rangle}$, $c = \rho(x)(1-\kappa\langle x,y\rangle)$, thus we obtain

$$c^*(y) = \sup_{x\in\Omega} \rho(x)(1-\kappa\langle x,y\rangle) \iff \frac{1}{c^*(y)} = \inf_{x\in\Omega} \frac{1}{\rho(x)(1-\kappa\langle x,y\rangle)}.$$

$1/c^*(y)$ is the function of y, denoted as $\eta : \Omega^* \to \mathbb{R}_+$.

Definition 2.23 (Generalized Legendre Transform)**.** Suppose ρ is an admissible function defined on Ω. The generalized Legendre transform of ρ with respect to the function $\frac{1}{1-\kappa\langle x,y\rangle}$ is a function η defined on the sphere $\mathbb{S}^2$ η, given by

$$\eta(y) = \inf_{x\in\Omega} \frac{1}{\rho(x)(1-\kappa\langle x,y\rangle)}. \tag{2.35}$$

2.5.3. Solution to refractor design Denote $\Omega^* = \partial\rho(\Omega)$. For any fixed point $y_0 \in \Omega^*$, (2.35) reaches the infimum at $x_0 \in \Omega$, then

$$\eta(y_0)\rho(x_0) = \frac{1}{1 - \kappa\langle x_0, y_0\rangle}, \tag{2.36}$$

For arbitrary $x \in \Omega$ and $y \in \Omega^*$,

$$\rho(x)\eta(y) \leq \frac{1}{1 - \kappa\langle x, y\rangle}. \tag{2.37}$$

we have

$$y_0 \in \partial\rho(x_0) \iff x_0 \in \partial\eta(y_0).$$

Especially, the generalized Legendre transform of η, restricted on Ω, is ρ itself,

$$\eta^{**} = \eta, \quad (\partial\eta)^{-1} = \partial\rho$$
$$\rho^{**} = \rho, \quad (\partial\rho)^{-1} = \partial\eta$$

Theorem 2.24. *Suppose Ω and Ω^* are domains in $\mathbb{S}^{n-1}$, the illumination intensity of the emanating ray lights is represented by a positive bounded function $f(x)$ defined on Ω, the illumination intensity of the refracted rays is represented by a positive bounded function $g(y)$ on $\overline{\Omega^*}$. Suppose $|\partial\Omega| = 0$ and satisfies the physical constraint*

$$\inf_{x\in\Omega, y\in\Omega^*} \langle x, y\rangle \geq \kappa. \tag{2.38}$$

furthermore, assume the total energy is conserved

$$\int_\Omega f(x)dx = \int_{\Omega^*} g(y)dy > 0, \tag{2.39}$$

where dx, dy represent the Hausdorff measure on $\mathbb{S}^{n-1}$. Then for $\kappa < 1$, there exists a week solution Γ_ρ, all such solutions Γ_ρ's differ by a scaling. □

Proof. By the (DP) theorem in optimal transportation, there are a pair of functions (ϕ, ψ), unique up to a constant, maximizing the following energy

$$\sup\{I(u, v) : (u, v) \in K\},$$

where

$$I(u,v) = \int_{\Omega} f(x)u(x)dx + \int_{\Omega^*} v(y)g(y)dy,$$
$$K = \left\{(u,v) \in (C(\overline{\Omega}), C(\overline{\Omega^*})) : u(x) + v(y) \leq c(c,y), \forall x \in \Omega, y \in \Omega^*\right\},$$
$$c(x,y) = -\log(1 - \kappa\langle x,y\rangle),$$

where $\langle x,y\rangle$ is the inner product in $\mathbb{R}^n$, such that $\rho = e^{\phi}$ is the solution to the spherical Monge-Ampère equation with the natural boundary condition. □

Theorem 2.25. *Suppose Ω and Ω^* are domains in $\mathbb{S}^{n-1}$, the illumination intensity of the emanating ray lights is represented by a positive bounded function $f(x)$ defined on Ω, the illumination intensity of the refracted rays is represented by a positive bounded function $g(y)$ on $\overline{\Omega^*}$. Suppose $|\partial\Omega| = 0$ and satisfies the physical constraint*

$$\inf_{x\in\Omega, y\in\Omega^*} \langle x,y\rangle \geq \frac{1}{\kappa}. \tag{2.40}$$

furthermore, assume the total energy is conserved

$$\int_{\Omega} f(x)dx = \int_{\Omega^*} g(y)dy > 0, \tag{2.41}$$

where dx, dy represent the Hausdorff measure on $\mathbb{S}^{n-1}$. Then for $\kappa > 1$, there exists a week solution Γ_ρ, all such solutions Γ_ρ's differ by a scaling. □

The proof is similar to the proof for the case of $\kappa < 1$, but the cost function is modified as

$$c(x,y) = -\log(\kappa\langle x,y\rangle - 1). \tag{2.42}$$

Fig. 15 shows one example of refractor designed using the proposed method. The refraction simulation result is shown, which is the prescribed Lena image.

2.6. Summary

From above discussion, we can see that the spherical optimal transportation map can be applied to solve the following fundamental problems:

1. Minkowski Problem I;
2. Reflector Design;

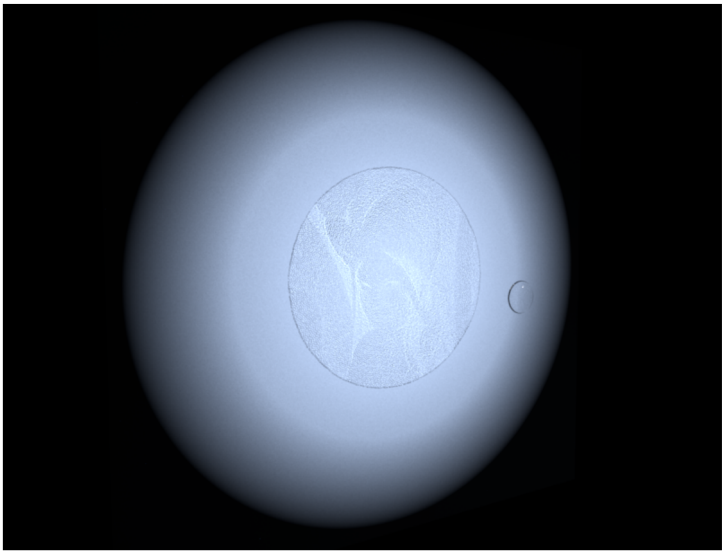

Figure 15: Reflector Design.

3. Refractor Design $\kappa < 1$;
4. Refractor Design $\kappa > 1$;

We compare the mathematical formulations for each problem. We use the following symbols: source measure (Ω, μ), target measure (Ω^*, ν), cost function $c(x, y)$, Kantorovich potential function (φ, ψ), density function $d\mu(x) = f(x)dx$, $d\nu(y) = g(y)dy$, the total transportation cost

$$\sup \left\{ \int_{\Omega} \varphi f + \int_{\Omega^*} \psi g : \varphi \oplus \psi \leq c \right\}$$

the c-transforms

$$\psi(y) = \varphi^c, \quad \varphi(x) = \psi^{\bar{c}}$$

The costs, support surfaces and the Brenier potentials, the Legendre duals and the optimal transportation maps are summarized in the following tables.

3. Computational algorithm

As shown in Fig. 16, the genus zero closed surface M is conformally mapped onto the unit sphere $\mathbb{S}^2$ using the spherical harmonic map algorithm [12].

	cost $c(x,y)$	support $c(x,y)-\psi(y)$	potential $\varphi=\inf_y c(x,y)-\psi(y)$
1	$\langle x,y\rangle$	$\langle x,y\rangle-\psi(y)$	$\varphi(x)=\sup_y\langle x,y\rangle-\psi(y)$
2	$-\log\langle x,y\rangle$	$\frac{e^{-\psi(y)}}{\langle x,y\rangle}$	$\rho(x)=e^{\varphi(x)}=\inf_y \frac{e^{-\psi(y)}}{\langle x,y\rangle}$
3	$-\log(1-\langle x,y\rangle)$	$\frac{e^{-\psi(y)}}{1-\langle x,y\rangle}$	$\rho(x)=e^{\varphi(x)}=\inf_y \frac{e^{-\psi(y)}}{1-\langle x,y\rangle}$
4	$-\log(1-\kappa\langle x,y\rangle)$	$\frac{e^{-\psi(y)}}{1-\kappa\langle x,y\rangle}$	$\rho(x)=e^{\varphi(x)}=\inf_y \frac{e^{-\psi(y)}}{1-\kappa\langle x,y\rangle}$
5	$-\log(\kappa\langle x,y\rangle-1)$	$\frac{e^{-\psi(y)}}{\kappa\langle x,y\rangle-1}$	$\rho(x)=e^{\varphi(x)}=\inf_y \frac{e^{-\psi(y)}}{\kappa\langle x,y\rangle-1}$

	map $\nabla_x c(x,T(x))=\nabla\varphi(x)$	support $c(x,y)-\psi(y)$	Legendre Dual $\psi(y)=\inf_x c(x,y)-\varphi(x)$
1	$T(x)=\nabla\varphi(x)$	plane	$\psi(y)=\sup_x\langle x,y\rangle-\varphi(x)$
2	$T(x)=n(x)$	plane	$\eta(y)=e^{\psi(y)}=\inf_x \frac{e^{-\varphi(x)}}{\langle x,y\rangle}$
3	$T(x)=x-2\langle x,n\rangle n$	paraboloid	$\eta(y)=e^{\psi(y)}=\inf_x \frac{e^{-\varphi(x)}}{1-\langle x,y\rangle}$
4	$n(x)=\frac{x-\kappa T(x)}{\lvert x-\kappa T(x)\rvert}$	ellipsoid	$\eta(y)=e^{\psi(y)}=\inf_x \frac{e^{-\varphi(x)}}{1-\kappa\langle x,y\rangle}$
5	$n(x)=\frac{x-\kappa T(x)}{\lvert x-\kappa T(x)\rvert}$	hyperboloid	$\eta(y)=e^{\psi(y)}=\inf_x \frac{e^{-\varphi(x)}}{\kappa\langle x,y\rangle-1}$

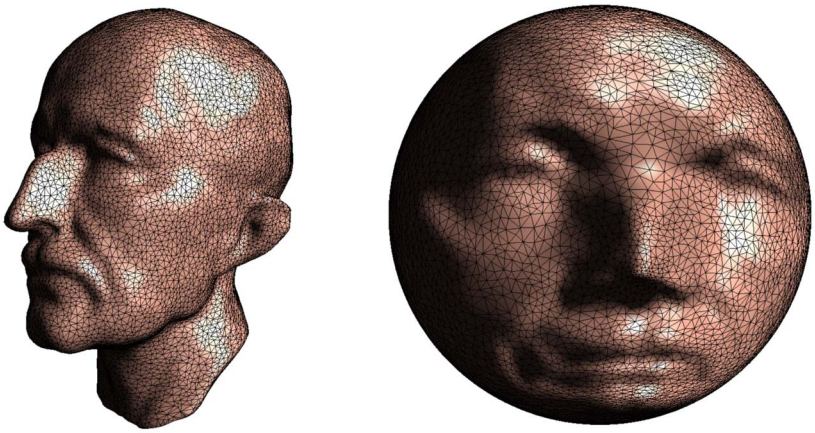

Figure 16: The Maxplanck surface (left) is conformally mapped onto the unit sphere by a harmonic map (right).

The image of each vertex $v_i \in M$ is $x_i \in \mathbb{S}^2$. The target measure ν_i equals to the one third of the total area of the faces adjacent to v_i. The target spherical measure is

$$\nu = \sum_{i=1}^{n} \nu_i \delta(x - x_i).$$

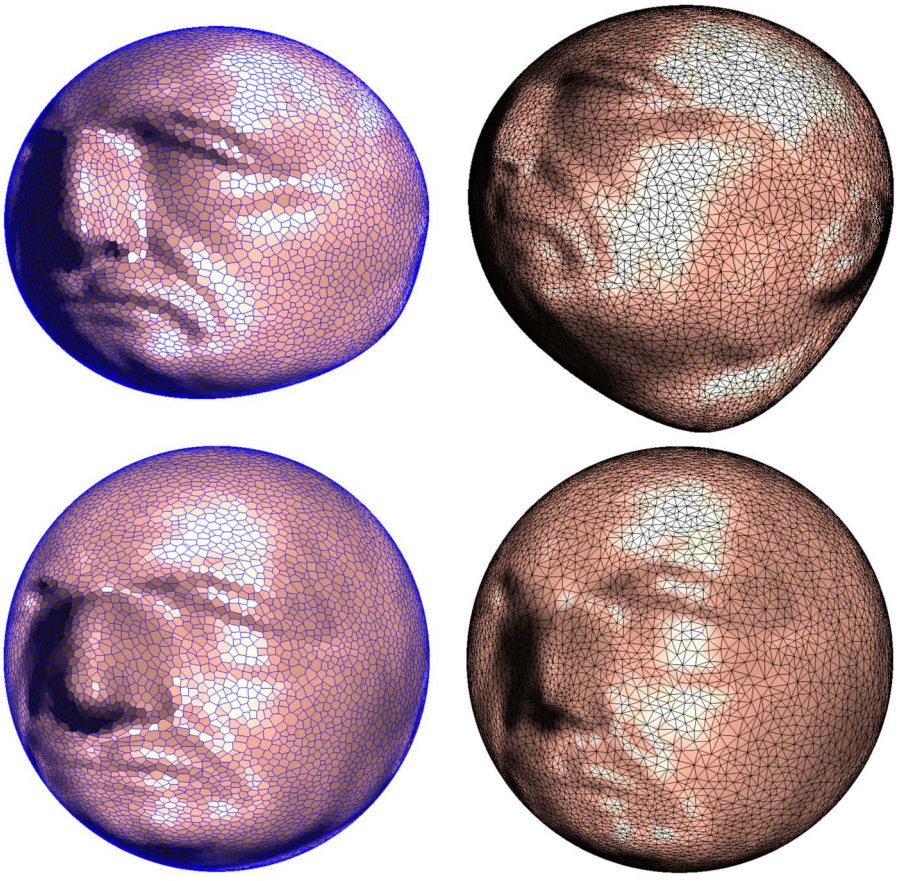

Figure 17: Spherical Legendre dual. The support plane $\rho(x) = h/\langle x, \mathbf{y}\rangle$ is dual to the point $h^{-1}\mathbf{y}$.

As shown in Fig. 17 top right frame, the Legendral dual of the Brenier potential is denoted as $\rho : \mathbb{S}^2 \to \mathbb{R}^+$, its radial graph is the convex hull of $\{\rho_i x_i\}$, which can be computed using Lawson Edge Flip algorithm [18]. In Fig. 17 top left frame, the spherical Brenier potential function is the Legendre dual of ρ, denoted as $1/\rho^*$. Each point $v_i = \rho_i x_i$ on the convex hull presents a plane $v_i^* = \pi_i$, its radial representation is

$$\pi_i(y) = \frac{1}{\rho_i} \frac{1}{\langle x_i, y\rangle}.$$

Each face on the convex hull $f = [\rho_i x_i, \rho_j x_j, \rho_k x_k]$ is dual to a vertex on the f^* on the spherical Brenior potential, which is the inner envelope of the

Algorithm 1: Spherical Power Diagram

Input: a set of points $\{\rho_i x_i\}_{i=1}^n$, a spherical convex domain Ω
Output: the spherical power diagram of $\{\rho_i x_i\}_{i=1}^n$
1. Compute the convex hull C of $\{\rho_i x_i\}_{i=1}^n$ using Lawson edge flipping Algorithm;
2. Compute the inner envelope of the planes $\{\pi_i(y)\}_{i=1}^n$ using spherical Legendral dual algorithm;
3. Central project the inner envelope onto the unit sphere to obtain the spherical power diagram $\mathcal{D}$;
4. Stereo-graphic project Ω and $\mathcal{D}$ onto the plane;
5. Clip the power cells using Sutherland-Hodgeman algorithm if necessary;
6. Stereo-graphic project back the clipped power cells onto the sphere.

supporting planes $\{\pi_i\}$, satisfying the condition

$$\langle \rho_i x_i, r^* \rangle = \langle \rho_j x_j, r^* \rangle = \langle \rho_k x_k, r^* \rangle.$$

In Fig. 17 lower left frame, the projection of the Brenier potential is a power diagram on the unit sphere. In the lower right frame, the projection of the Legendre dual of the Brenier potential is a Weighted Delaunay triangulation of the sphere. The details for the spherical power diagram algorithm can be found in Alg. 1.

Assume μ is the source measure on the sphere $\mu(\mathbb{S}^2) = 4\pi$, with continuous density function. The target measure is $\nu = \sum_{i=1}^n \nu_i \delta(y - y_i)$. The spherical power diagram is $\mathbb{S}^2 = \bigcup_{i=1}^n W_i(\eta)$, the measure of each cell is $w_i(\eta) = \mu(W_i(\eta))$. The Kantorovich potentials are $\varphi = \log \rho$ and $\psi = \log \eta$, the functional is

$$\begin{aligned} I(\varphi, \psi) &= \int_{\mathbb{S}^2} \varphi(x) d\mu(x) + \int_{\mathbb{S}^2} \psi(y) d\nu(y), \quad \varphi \oplus \psi \leq c \\ &= \sum_{i=1}^n \int_{W_i(\psi)} \psi^c d\mu(x) + \sum_{i=1}^n \psi_i \nu_i, \quad \psi_i = \psi(y_i) \\ &= \sum_{i=1}^n \int_{W_i(\psi)} (c(x, y_i) - \psi_i) d\mu(x) + \sum_{i=1}^n \psi_i \nu_i. \end{aligned}$$

Let $\psi = (\psi_1, \psi_2, \ldots, \psi_n)$, $c(x, y) = -\log\langle x, y \rangle$, the energy

$$I(\psi) = \sum_{i=1}^n \int_{W_i(\psi)} (c(x, y_i) - \psi_i) d\mu(x) + \sum_{i=1}^n \psi_i \nu_i.$$

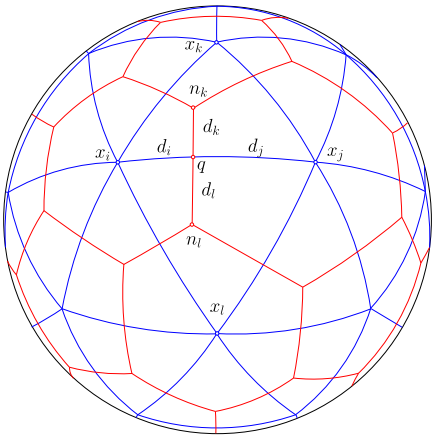

Figure 18: The duality between the spherical power diagram and the weighted Delaunay triangulation.

The gradient is

$$\nabla I(\psi) = (\nu_1 - w_1(\psi), \nu_2 - w_2(\psi), \cdots, \nu_n - w_n(\psi)).$$

As shown in Fig. 18, the spherical power digram and the spherical weighted Delaunay triangulation are dual to each other. The Hessian matrix equals to

$$\begin{cases} \dfrac{\partial^2 I(\psi)}{\partial \psi_i \partial \psi_j} = -\dfrac{\partial w_i(\psi)}{\partial \psi_j} = -\dfrac{\partial w_j(\psi)}{\partial \psi_i} = \dfrac{\sin d_l + \sin d_k}{\tan d_i + \tan d_j} \\ \dfrac{\partial^2 I(\psi)}{\partial \psi_i^2} = \displaystyle\sum_{i \neq j} \frac{\partial w_i(\psi)}{\partial \psi_j} \end{cases}$$

The null space of the Hessian matrix is $\mathrm{Span}\{(1, 1, \ldots, 1)\}$. The energy is strictly concave in the subspace $\sum_{i=1}^{n} \psi_i = 0$. During the optimization, we have to make sure the Brenier potential is non-degenerated, all the power cells are non-empty. We adapted a damping algorithm to guarantee the non-degeneracy. Suppose at the current stage, the Brenier potential is legal, we update the radial length by d, if some cells disappear in the power diagram, we return to the initial stage, and change the radial change by $d/2$. We repeat this trial procedure until find the appropriate radial change d. Algorithmic details can be found in Alg. 2. Based on the damping algorithm, we can design the Newton's algorithm for the optimization. The Newton's algorithm is explained in Alg. 3.

Algorithm 2: Spherical Damping

Input: a set of points $\{\rho_i x_i\}_{i=1}^n$, a radial change d

Output: the updated spherical power diagram of $\{\rho_i e^{\lambda d_i} x_i\}_{i=1}^n$ for some λ, such that no power cell is degenerated

1. Initialize the step length λ;
2. $\rho_i \leftarrow \rho_i e^{\lambda d_i}$;
3. Compute the convex hull using spherical Lawson edge flipping Algorithm [18];
4. If the convex hull misses any vertex, then $\lambda \leftarrow \frac{1}{2}\lambda$, repeat step 2 and step 3;
5. Compute the upper envelope using Legendre dual algorithm, project to the spherical power diagram $\mathcal{D}$;
6. If necessary, clip the power cells using Sutherland-Hodgman algorithm [26];
7. If any power cell is empty, then $\lambda \leftarrow \frac{1}{2}\lambda$, repeat step 2 through step 6;

Algorithm 3: Spherical Newton's Method

Input: $\{x_i\}_{i=1}^n \subset \mathbb{S}^2$, $\{\nu_i\}_{i=1}^n$, $\sum_{i=1}^n \nu_i = 4\pi$, $\nu_i > 0$

Output: Convex hull of $\{\rho_i x_i\}_{i=1}^n$, such that the curvature at $\rho_i x_i$ is ν_i

1. Initialize ρ as $\rho_i \leftarrow 1$;
2. Call the spherical power diagram Alg. 1;
3. Compute the gradient ∇E, the target area minus the current power cell area;
4. Compute the Hessian matrix H, using the power diagram edge length;
5. Compute the update direction $Hd = \nabla E$;
6. Call the spherical damping Alg. 2, set $\rho \leftarrow \rho e^{\lambda d}$, such that ρ is admissible;
7. Repeat step 2 through step 6, until the gradient is close to 0.

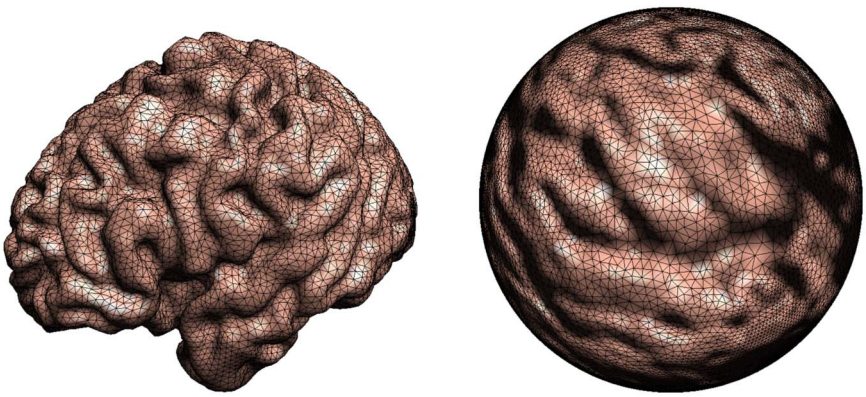

Figure 19: The initial conformal map from the cortical surface to the unit sphere.

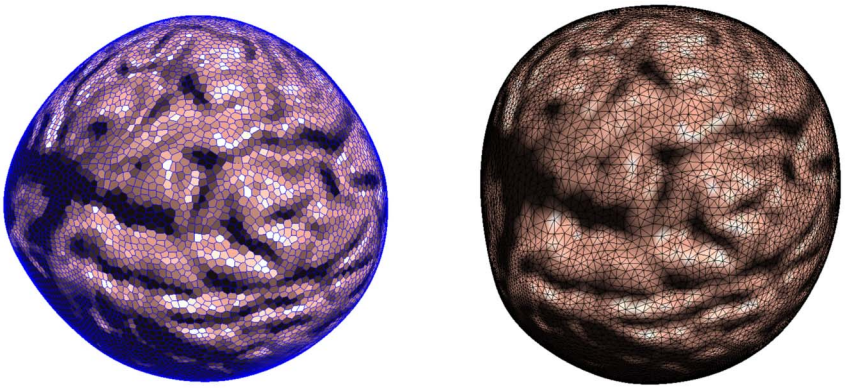

Figure 20: The Brenier potential and the Legendre dual functions.

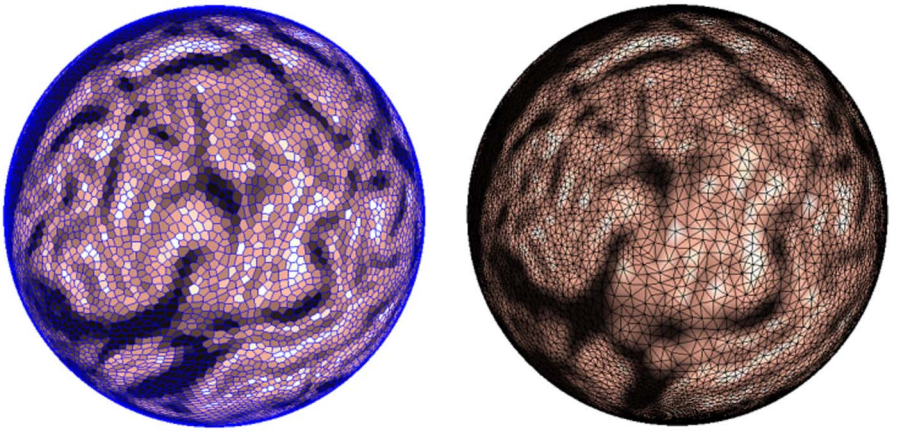

Figure 21: The spherical power diagram and the spherical weighted Delaunay triangulation. The spherical optimal transport map is given by mapping each power cell to the corresponding vertex in the weighted Delaunay triangulation.

Fig. 19 shows a human cortical surface (left), which is conformally mapped onto the unit sphere using a harmonic map (right). Fig. 20 shows the Brenier potential (left) and its Legendral due (right). Fig. 21 shows the spherical power diagram (left) and the spherical weighted Delaunay triangulation (right). The spherical optimal transport map is given by mapping each power cell to the dual vertex.

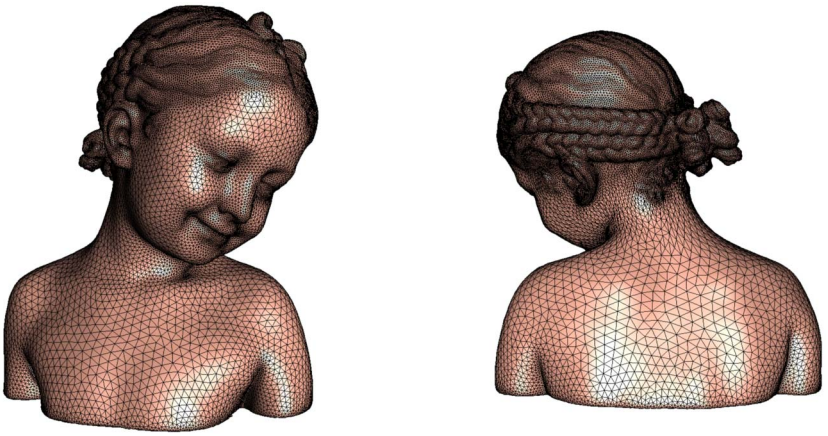

Figure 22: Input meshes.

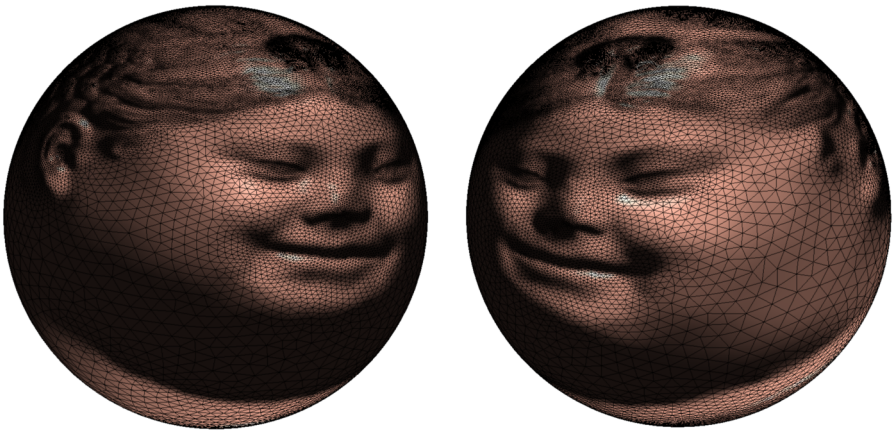

Figure 23: Initial harmonic maps.

Fig. 22 shows the input Bimba surface, Fig. 23 shows the spherical harmonic map, Fig. 24 and Fig. 25 show the Brenier potential and the Legendral due for the optimal transportation map.

Acknowledgement

The work of Luo is supported in part by NSF 1760527. The work of Gu is supported in part by NIH 3R01LM012434-05S1, 1R21EB029733-01A1, NSF FAIN-2115095 and NSF CMMI-1762287. The work of Lei is partially

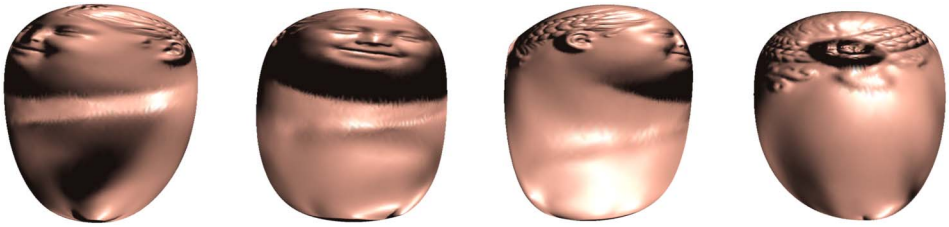

Figure 24: The Legendre dual of the Brenier potential.

Figure 25: The Brenier potential.

supported by National Key R&D Program of China 2021YFA1003003 and NSFC No. 61936002, T2225012.

References

[1] An, D., Xie, J. and Li, P. (2021). Learning Deep Generative Models by Short-run MCMC Inference with Optimal Transport Correction. In *Conference on Computer Vision and Pattern Recognition (CVPR)*.

[2] An, D., Guo, Y., Lei, N., Luo, Z., Yau, S.-T. and Gu, X. (2020a). AE-OT: A new Generative Model based on extended semi-discrete optimal transport. In *International Conference on Learning Representations*.

[3] An, D., Guo, Y., Zhang, M., Qi, X., Lei, N. and Gu, X. (2020b). AE-OT-GAN: Training GANs from data specific latent distribution. In *ECCV*.

[4] Arjovsky, M., Chintala, S. and Bottou, L. (2017). Wasserstein generative adversarial networks. In *ICML* 214–223.

[5] Bentley, J. L. and Ottmann, T. A. (1979). Algorithms for reporting and counting geometric intersections. *IEEE Transactions on Computers* **C-28** 643–647.

[6] Berg, M. d., Cheong, O., Kreveld, M. v. and Overmars, M. (2008). *Computational Geometry: Algorithms and Applications*, 3rd ed. ed. Springer-Verlag TELOS, Santa Clara, CA, USA. MR2723879

[7] Brenier, Y. (1991). Polar factorization and monotone rearrangement of vector-valued functions. *Comm. Pure Appl. Math.* **44** 375–417. MR1100809

[8] Courty, N., Flamary, R., Tuia, D. and Rakotomamonjy, A. (2017). Optimal Transport for Domain Adaptation. *IEEE Transactions on Pattern Analysis and Machine Intelligence* **39** 1853–1865.

[9] Delon, J. (2004). Midway image equalization. *J. Math. Imaging Vision*. MR2090128

[10] Galichon, A. (2016). *Optimal Transport Methods in Economics*. Princeton University Press. MR3586373

[11] Glimm, T. and Oliker, V. (2003). Optical design of single reflector systems and the Monge–Kantorovich mass transfer problem. *Journal of Mathematical Sciences* **117** 4096–4108. MR2027449

[12] Gu, X., Wang, Y., Chan, T. F., Thompson, P. M. and Yau, S.-T. (2004). Genus zero surface conformal mapping and its application to brain surface mapping. *IEEE Transactions on Medical Imaging (TMI)* **23** 949–958.

[13] Gu, D. X., Luo, F., Sun, J. and Yau, S.-T. (2016). Variational principles for Minkowski type problems, discrete optimal transport, and discrete Monge-Ampère equations. *Asian Journal of Mathematics* **20** 383–398. MR3480024

[14] Haber, E., Rehman, T. and Tannenbaum, A. (2010). An efficient numerical method for the solution of the l2 optimal mass transfer problem. *SIAM J. Sci. Comput.* **32** 197–711. MR2599774

[15] Haker, S., Zhu, L., Tannenbaum, A. and Angenent, S. (2004). Optimal Mass Transport for Registration and Warping. *International Journal of Computer Vision* **60** 225–540.

[16] Kusner, M., Sun, Y., Kolkin, N. and Weinberger, K. (2015). From word embeddings to document distances. In *Proceedings of the 32nd International Conference on Machine Learning* 957–966.

[17] Lai, R. and Zhao, H. (2017). Multiscale Nonrigid Point Cloud Registration Using Rotation-Invariant Sliced-Wasserstein Distance via Laplace–Beltrami Eigenmap. *SIAM Journal on Imaging Sciences* **10** 449–483. MR3631386

[18] Lawson, C. L. (1972). Transforming triangulations. *Discrete Mathematics*. MR0311491

[19] Lei, N. and Gu, X. (2021). *Optimal Transportation Theory and Computation*. Higher Education Press.

[20] Miyato, T., Kataoka, T., Koyama, M. and Yoshida, Y. (2018). Spectral normalization for generative adversarial networks. In *ICLR*.

[21] Nguyen, X. (2013). Convergence of latent mixing measures in finite and infinite mixture models. *Ann. Statist* **41** 370–400. MR3059422

[22] Pitie, F., Kokaram, A. C. and Dahyot, R. (2007). Automated colour grading using colour distribution transfer. *Computer Vision and Image Understanding* **107** 123–137.

[23] Rabin, J., Ferradans, S. and Papadakis, N. (2014). Adaptive color transfer with relaxed optimal transport.

[24] Schiebinger, G., Shu, J., Tabaka, M., Cleary, B., Subramanian, V., Solomon, A., Gould, J., Liu, S., Lin, S., Berube, P., Lee, L., Chen, J., Brumbaugh, J., Rigollet, P., Hochedlinger, K., Jaenisch, R., Regev, A. and Lander, E. (2019). Optimal-Transport Analysis of Single-Cell Gene Expression Identifies Developmental Trajectories in Reprogramming. *Cell* **176** 928–943.

[25] Su, Z., Wang, Y., Shi, R., Zeng, W., Sun, J., Luo, F. and Gu, X. (2015). Optimal Mass Transport for Shape Matching and Comparison. *IEEE Transactions on Pattern Analysis and Machine Intelligence* **37** 2246–2259.

[26] Sutherland, I. and Hodgman, G. W. (1974). Reentrant Polygon Clipping. *Communications of the ACM* **17** 32–42.

[27] Tolstikhin, I., Bousquet, O., Gelly, S. and Schoelkopf, B. (2018). Wasserstein Auto-Encoders. In *ICLR*.

[28] Villani, C. (2003). *Topics in Optimal Transportation* **58**. American Mathematical Society. MR1964483

[29] Villani, C. (2008). *Optimal transport: old and new* **338**. Springer Science & Business Media. MR2459454

[30] Yurochkin, M., Claici, S., Chien, E., Mirzazadeh, F. and Solomon, J. M. (2019). Hierarchical Optimal Transport for Document Representation. In *Advances in Neural Information Processing Systems 32*.

[31] Zhang, M., An, D., Lei, N., Wu, J., Zhao, T., Xu, X., Wang, Y. and Gu, X. (2021). Cortical Morphometry Analysis based on Worst Transportation Theory. In *International Conference on Information Processing in Medical Imaging* 163–176. Springer, Cham.

[32] Zhao, X., Su, Z., Gu, X. D., Kaufman, A., Sun, J., Gao, J. and Luo, F. (2013). Area-preservation mapping using optimal mass transport. *IEEE Transactions on Visualization and Computer Graphics* **19** 2838–2847.

Zhou Zhao
State University of New York at Stony Brook
E-mail address: zhozhao@cs.stonybrook.edu

Na Lei
Dalian University of Technology
E-mail address: nalei@dlut.edu.cn

Li Cui
Beijing Normal University
E-mail address: licui@bnu.edu.cn

Kehua Su
Wuhan University
E-mail address: skh@whu.edu.cn

Xiaoyin Xu
Harvard University
E-mail address: xxu@bwh.harvard.edu

Feng Luo
Rutgers University
E-mail address: fluo@math.rutgers.edu

Xianfeng Gu
State University of New York at Stony Brook
E-mail address: gu@cs.stonybrook.edu

Shing-Tung Yau
Tsinghua University
Harvard University
E-mail address: yau@math.harvard.edu

Received July 5, 2022